TASK QUARTERLY 5 No 4 (2001), 433–458

NUMERICAL SIMULATION AND THEORETICAL ANALYSIS OF THE 3D VISCOUS FLOW IN CENTRIFUGAL IMPELLERS

SHUN KANG AND CHARLES HIRSCH

Vrije Universiteit Brussels,
Department of Fluid Mechanics,
Pleinlaan 2, 1050 Brussels, Belgium
kang@stro.vub.ac.be

(Received 20 July 2001)

Abstract: This paper investigates the three-dimensional viscous flow in centrifugal impellers through theoretical analysis and numerical simulations, which is a summary of the authors' recent work. A quantitative evaluation of the different contributions to the streamwise vorticity is performed, namely, the passage vortices along the endwalls due to the flow turning; a passage vortex generated by the Coriolis forces proportional to the local loading and mainly active in the radial parts of the impeller; blade surface vortices due to the meridional curvature. In the numerical simulation the NASA Large Scale Centrifugal Compressor (LSCC) impeller with vaneless diffuser is computed at three flow rates. An advanced Navier-Stokes solver, EURANUS/TURBO is applied with an algebraic turbulence model of Badwin-Lomax and a linear k-ε model for closure, for different meshes. An in-depth validation has been performed based on the measured data. An excellent agreement is obtained for most of the data over a wide region of the flow passage. Structures of the 3D flow in the blade passage and the tip region, and their variations with flow rate as well, are analysed based on the numerical results.

Keywords: centrifugal compressor, secondary flow, CFD, tip leakage flows, viscous flow

Nomenclature

C_p – specific heat at constant pressure
p – static pressure, N/m^2
p^* – rotary stagnation pressure, N/m^2
P_r – reduced static pressure, N/m^2
P_{ref} – reference pressure, N/m^2
P_{ao} – absolute total pressure, N/m^2
PS – pressure side
Ro – Rossby number
SS – suction side
T_{ao} – static temperature, K
T_u – turbulence intensity
U – rotor blade speed, m/s
V_m – throughflow velocity, m/s
V_θ – tangential absolute velocity, m/s

V_z – axial absolute velocity, m/s
W – relative velocity, m/s
β – relative flow angle
δ – boundary layer thickness, m
μ_l – moleculor viscosity, m^2/s
μ_t – turbulent viscosity, m^2/s
ρ – density, kg/m^3
σ – meridional flow angle
ω – rotation speed, 1/s
ω_s – streamwise vorticity, 1/s

1. Introduction

In recent years, the 3D flow structure of axial turbines and compressors has been the subject of numerous experimental and computational studies and a clear picture has emerged, recognising the effects of horseshoe vortex, passage vortex and endwall corner separation on the suction surface in the trailing edge region. Many researchers have contributed to this present state of knowledge. Out of an arbitrary selection, containing also references to earlier work, we can refer to [1, 2], for turbine blade rows, to [3–5] for compressor blade rows. Figure 1 presents a schematic view of the secondary flow structure in a compressor cascade with tip clearance [6]. It shows that a horseshoe vortex (HV) forms in front of the blade leading edge, with its pressure side leg (HVp) being merged together with the passage vortex (PV) downstream. This vortex is generated due to the endwall boundary layer and blade curvature.

On the other hand, centrifugal compressor flows have still many open questions left and the amount of detailed information concerning their 3D flow structure is still rather fragmented. This is largely due to the considerable difficulty in obtaining detailed flow data in the complex flow channels of centrifugal impellers, characterised by long twisted 3D passages of high curvature and low aspect ratio. Based on earlier scarce data, a significant progress in understanding of centrifugal compressor and pump flows has been obtained from the jet/wake concept introduced by Bob Dean and his coworkers [8, 9], in the early seventies. This model refers essentially to the existence of a low speed, low energy region of separated flow along the suction side in the downstream part of the impeller, created by the strong diffusion and subsequent boundary layer growth. The remarkable experiments of Eckardt [10], applying for the first time laser anemometry to measure the relative flow in an impeller, provided a spectacular confirmation of the presence of a wake region, although its relation to a blade-to-blade separation was not clearly confirmed. Figure 2 shows the throughflow velocity profiles at the impeller exit [7], in which the jet/wake profile is seen. Other experimental investigations, in particular [11, 12] provided additional insight into some of the secondary flow mechanisms in centrifugal compressor channels. In the experimental results of Krain [13], low velocity regions are found near the shroud, somewhat midway between the blade surfaces, leading to smooth velocity profiles, not quite like the sharp transition from the high to low velocity region in Figure 2.

Simultaneously, from 1980 on, results from Navier-Stokes computations have been attempting to provide additional insight into the complex flow structure of centrifugal impeller passages. The first reported computations of the Eckardt impeller were performed by Moore and Moore [14] with, by today's standards, an extremely coarse mesh of the order of $13 \times 14 \times 25 = 4550$ points, including the tip clearance. Despite this, qualitative indications

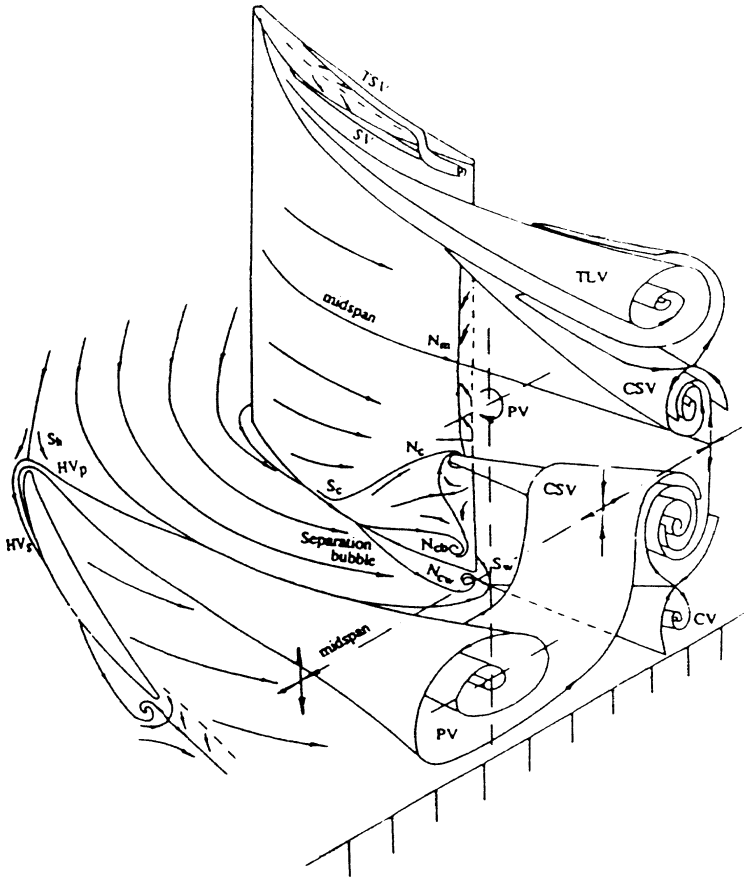

Figure 1. Schematic of secondary flow structure in a compressor cascade with tip clearance, Kang [6]: PV – Passage vortex; HV – Horseshoe vortex; TLV – Tip leakage vortex; TSV – Tip secondary vortex; SV – Secondary vortex; CSV – Concentrated shed vortex; CV – Corner vortex

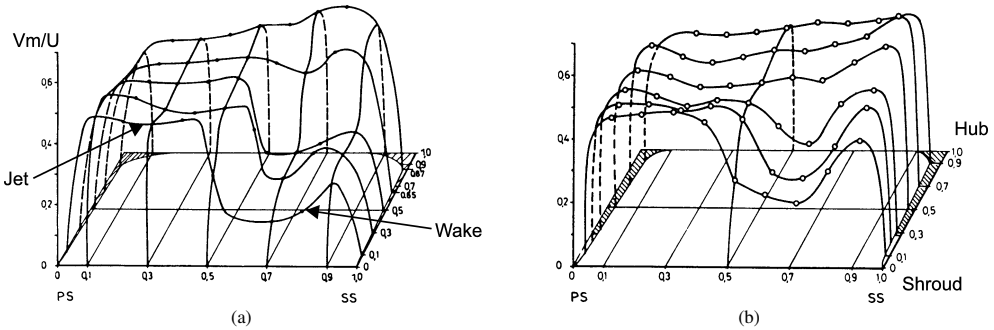

Figure 2. Throughflow velocity at the exit of Eckardt's impeller, Eckardt [7]: (a) radial; (b) backswept 30°

of the formation of a wake-type region were obtained. Other efforts, such as [15], showed results of the 3D viscous flow in an industrial centrifugal compressor by using the CFD codes of Denton [16] and Dawes [17], with meshes of the order of 25 000 points. Despite the large differences in the numerical methods, the casing boundary conditions and the

turbulence models, both codes predicted similar flow fields. Dawes [18] simulated the 3D unsteady viscous flow in a centrifugal compressor with a vaned diffuser and found that the impeller flow is essentially steady with a limited influence from the diffuser, vaned or not. These and other computations, such as [19], showed that the gross features of the impeller flows can be captured by the Navier-Stokes computations, even on relatively coarse meshes and simple turbulence models.

However, if CFD is to be applied as a *quantitative* tool, to compensate for the near impossibility of obtaining detailed experimental data of boundary layer and secondary flows in the complex flow channels of centrifugal machines, more severe requirements have to be put on the CFD computations and results. In particular, since the secondary flow intensity is directly related to the stagnation pressure gradients in the boundary layers, sufficient grid resolution has to be provided in order to capture accurately the intensity of the secondary flows.

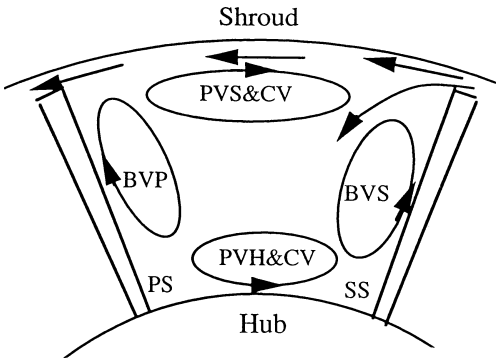

Figure 3. Combination of passage and blade vortices PVS & PVH – passage vortices at shroud and hub; BVS & BVP – blade surface vortices at SS and PS; CV – Coriolis passage vortex

This jet/wake flow pattern, separates high from low velocity fluid, resulting in accumulation of low energy fluid in the shroud/suction side area and collection of high energy fluid in the hub/pressure side area. The main progress of this model lies in the recognition that viscous and secondary flow phenomena have turned the largely inviscid dominated inlet flow field, with its high velocity region along the shroud/suction surfaces, into an exit flow where the sign of the velocity gradients has been reversed, namely high speeds along the pressure surface and lower speeds in the shroud/suction side region. It has been found, however, that the position of the wake (low energy region) is not always located in the shroud/SS corner but changes with the impeller geometry and Rossby number. As reported by Eckardt [7], Figure 2, the wake in an impeller with a radial exit angle is in the shroud/SS corner, while for an impeller with backswept blades it is away from the corner. Johnson and Moore [20] found, from their experimental studies in a shrouded impeller with radial discharge, that the wake is shifting towards the pressure side with increasing flow rate. A similar observation has been reported by Chriss *et al.* [21] and Kang and Hirsch [22]. Hirsch *et al.* [23, 24] concluded, in analysing the numerical and experimental data of a high subsonic compressor impeller and a low speed pump impeller, that the location of the wake results from a balance between the various secondary vortices, and the tip leakage flow. A sketch of the different components of the secondary vortices is shown in Figure 3. It

consists essentially of the endwall passage vortex, PV, generated by the endwall boundary layers and the blade-to-blade streamline curvature, the blade surface vortex, BV, due to the meridional curvature of the flow channel and the blade surface boundary layers, and CV due to the Coriolis force and the endwall boundary layers in the radial parts.

In the last few years, the authors and his colleagues have been working on the CFD simulation and analysis of the 3D viscous flows in centrifugal impellers, including Krain impeller, SHF pump impeller and LSCC impeller [23–26, 22]. Validations presented in these papers have shown excellent agreement with the available experimental data, on meshes fine enough to resolve the wall boundary layers. Analysies of the computed and experimental data have given insight into the basic mechanisms of flow features leading to the formation of the jet/wake flow structure in centrifugal machines.

This paper presents a summary of our work in the investigation of the three-dimensional viscous flows in centrifugal impeller through theoretical analysis and numerical simulation. In theoretical analysis, a quantitative evolution of the different contributions to the streamwise vorticity will be performed. In the numerical simulation the CFD data for NASA Large Scale Centrifugal Compressor (LSCC) impeller with vaneless diffuser will be presented for three flow rate conditions. The Navier-Stokes solver, EURANUS/TURBO, is applied with an algebraic turbulence model of Badwin-Lomax and a linear k-ε model for closure. Comparison with experimental data will be given. Structures of the 3D flow in the blade passage and the tip region, and their variations with flow rate as well, will be analysed based on the numerical results.

2. Analysis of the secondary flow in centrifugal impeller

2.1. The basic forces on impeller flows

The inviscid balance of forces equals the pressure gradient to the sum of the inertia and the centrifugal forces resulting from the flow turning plus the centrifugal forces due to the rotation and the Coriolis force. In a blade-to-blade surface generated by the rotation of the meridional streamline m with angle σ to the axial direction, Figure 4, the balance of forces can be expressed in the streamline coordinates (s,n,b), where s is along the streamline, n is normal to the streamline in the blade-to-blade surface and b is the binormal perpendicular to s and n:

$$\frac{1}{\rho}\vec{\nabla}p = -W\frac{\partial W}{\partial s}\vec{l}_s \pm \frac{W^2}{R_b}\vec{l}_n + \omega^2\vec{r} - 2\omega W\sin\sigma\vec{l}_n \tag{1}$$

The first term on the right hand side is the streamwise inertia force, while the second term is the centrifugal force due to the curvature. The positive sign of this term corresponds to a convex streamline, while the negative sign corresponds to a concave streamline. The third and fourth terms correspond to the centrifugal and Coriolis forces.

In the blade-to-blade surface with backswept blades, the radius of the curvature, R_b, is generally very large and the Coriolis term dominates the centrifugal term, (for radial blades $\sin\beta$ is close to zero and when looking at the pressure gradients in the θ direction the centrifugal term does not contribute). Hence, a transverse pressure gradient is generated with the high pressure on the pressure side due essentially to the Coriolis force term. In the inducer part, where the meridional angle σ is small, the curvature term is directed towards the pressure surface and is responsible for the transverse pressure gradient towards the pressure side.

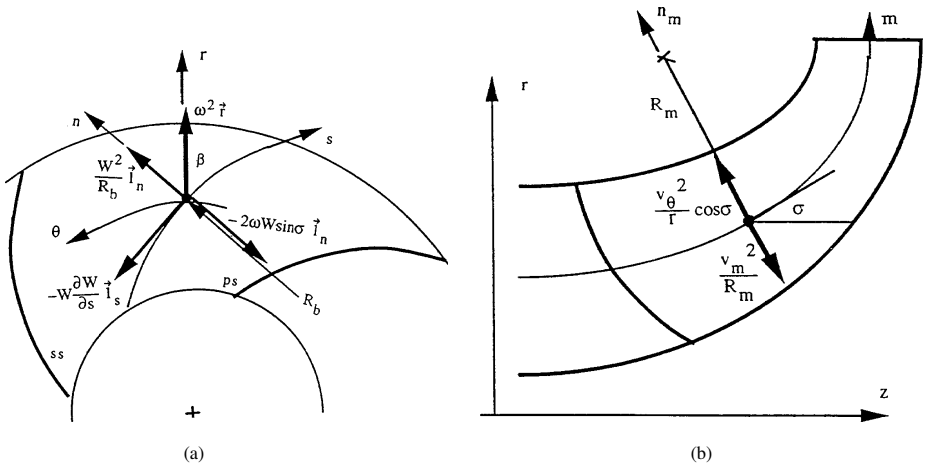

Figure 4. Inviscid forces in a rotating impeller: (a) cross section and (b) meridional section

In the meridional section, where the curvature $1/R_m$ is large in the inducer and inlet regions of impellers, while the absolute tangential velocity V_θ is small, a pressure gradient from shroud to hub balances the centrifugal force due to the meridional curvature. The normal balance of forces along n_m leads to:

$$\frac{1}{\rho}\frac{\partial p}{\partial n_m} = \frac{V_\theta^2}{r}\cos\sigma - \frac{V_m^2}{R_m} \tag{2}$$

Hence, the invicid balance of forces leads to a velocity increase from hub to shroud and from the pressure to suction side in a nearly linear variation. The iso-velocity lines are therefore oriented from the suction side/hub to the shroud/pressure side corner, being closed in the boundary layers. The impeller flow will be controlled by the inviscid forces in the inlet region, where viscous effects are not yet developed. In the radial parts of the impeller both terms on the right hand side of Equation (2) will become very small and tend to zero.

2.2. Secondary flow components

It is known from the basic studies [27, 11, 15], as also confirmed by the analysis of Hirsch *et al.* [23], that the viscous effects progressively dominate the flow behavior when moving downstream in the impeller. An appropriate way of understanding the various flow contributions, due to viscous effects, is to follow the rate of increase of streamwise vorticity, describing the secondary flows generated by the rotary stagnation pressure gradients in the boundary layers, see *e.g.* [28]. This relation was derived initially by Hawthorne in 1974 in an unpublished report, and can also be found in [29]. This basic relation is expressed as follows, by relating the variation of streamwise vorticity with the rotary stagnation pressure $p^* = p + \rho W^2/2 - \rho u^2/2$:

$$\frac{\partial}{\partial s}\left[\frac{\Omega_s}{W}\right] = \frac{2}{\rho W^2}\left[\frac{1}{R_n}\frac{\partial p^*}{\partial b} + \frac{\omega}{W}\frac{\partial p^*}{\partial z}\right] \tag{3}$$

where R_n is the radius of curvature in the direction n, normal to the streamline. The first term is responsible for the passage vortices due to flow turning, while the second term has its origin in the Coriolis forces. Other vortices, having a local influence on the flow, such as horseshoe, corner and tip clearance vortices, are not described by Equation (3).

Due to the geometry of centrifugal impellers, the blade-to-blade curvature will generate secondary flow due to the hub and shroud boundary layers (the passage vortices, PV), Figure 3, while the meridional curvature will induce secondary flows due to the boundary layers developing along the blade surfaces (the blade surface vortices, BV). The second term, originating from the Coriolis forces, will be effective if a boundary layer gradient exists in the axial direction. This will be the case for the endwall boundary layer in the radial parts of the impeller, where they will be contributing to the passage vortices (Coriolis passage vortices, CV). If the inducer blade geometry is at an angle to the axial direction, the blade boundary layers will contribute an axial component of the blade stagnation pressure loss gradients. This contribution is expected to be small and will not be considered here.

The passage vortices drive low energy fluid from the pressure towards the suction surface along hub and shroud walls, while the blade surface vortices generate flow components along the blade surfaces from hub to shroud. The resulting motion leads to an accumulation of low velocity, high loss fluid towards the suction surface region, called the wake region. The resulting position of this wake region will depend on the balance between these different vortices.

The intensity of individual vortices shown in Figure 3 can then be estimated from Equation (3) following [24], considering that the reduced static pressure $[p-\rho(r\omega)^2/2]$ does not vary significantly in the boundary layers.

2.2.1. Passage vortex from blade-to-blade curvature

This curvature will generate the endwall vortex PVs and PVh, due to the endwall boundary layers. The intensity of these vortices can be obtained from Equation (3) as:

$$d\left[\frac{\Omega_s}{W}\right]_{PV/h,s} = \frac{2}{W}\frac{1}{R_b}\left[\frac{\partial W}{\partial b}\right]_{h,s} ds = \frac{2}{W}\left[\frac{\partial W}{\partial b}\right]_{h,s} d\beta \tag{4}$$

where $d\beta = ds/R_b$. Hence, the contribution will vanish locally for radial ending blades, in absence of backsweep. This equation can also be approximately expressed in another way as:

$$d\left[\frac{\Omega_s}{W}\right]_{PV/h,s} = \frac{2}{W}\frac{1}{R_b}\left[\frac{\partial W}{\partial b}\right]_{h,s} ds \approx \frac{2}{W}\frac{1}{R_b}\frac{W}{\delta_{h,s}} ds \approx \frac{2}{R_b}\frac{ds}{\delta_{h,s}} \tag{5}$$

where $\delta_{h,s}$ is the thickness of hub and shroud boundary layers and R_b the curvature radius of streamlines in the blade-to-blade surface.

2.2.2. Blade surface vortices

In a similar way, the intensity of the blade surface vortices BV can be estimated, leading to:

$$d\left[\frac{\Omega_s}{W}\right]_{BV/ps,ss} = \frac{2}{W}\frac{1}{R_m}\left[\frac{\partial W}{\partial b}\right]_{ps,ss} ds \approx \frac{2}{R_m}\frac{ds}{\delta_{\mathrm{PS,SS}}} \tag{6}$$

where $\delta_{\mathrm{PS,SS}}$ is the thickness of hub and shroud boundary layer and R_m the curvature radius of streamlines in the meridional surface. It can be seen that increasing the channel curvature $1/R_m$ increases the blade surface vortices. This contribution will not grow in the radial parts of impellers, where $1/R_m$ tends to zero.

2.2.3. Passage vortices from Coriolis forces

The second term of Equation (3) is significant where the hub and shroud normals have axial components, that is in the radial portions of the impeller. The Coriolis vortex CV can be estimated from Equation (3) as:

$$d\left[\frac{\Omega_s}{W}\right]_{CV/h,s} = \frac{2}{\rho W_2}\frac{\omega}{W}\left[\frac{\partial p^*}{\partial z}\right] \approx \frac{\omega}{W}\frac{ds}{\delta_{h,s}} \tag{7}$$

Or, as in [24], it can also be expressed as:

$$d\left[\frac{\Omega_s}{W}\right]_{CV/h,s} = \frac{2}{W_m}\frac{\Delta W_{ps}}{p\delta_{h,s}}ds \tag{8}$$

where p is the pitch. It can be seen that the contribution to the passage vortex variation is proportional to the loading ΔW_{ps} and inversely proportional to the meridional velocity, that is to mass flow rate. In other words, the intensity of the vortex CV is proportional to the rotationaly speed as this loading is produced by the Coriolis effect but not the blade-to-blade curvature. This component of the secondary flow will tend to become dominant in the radial parts of impellers.

2.2.4. Balance of the vortices

The location, size, and the level of energy loss, of the wake depend on the balance of all these vortices. This balance can be described by the ratio of the streamwise increments of the passage vortex (PV and CV) to the blade surface vortex (BV), leading to:

$$\left|\frac{d\left[\frac{\Omega_s}{W}\right]_{h,s} + d\left[\frac{\Omega_s}{W}\right]_{CV}}{d\left[\frac{\Omega_s}{W}\right]_{BV}}\right| \approx \frac{\delta_{\mathrm{PS,SS}}}{\delta_{h,s}}\left(\frac{R_m}{R_b} + \frac{\omega R_m}{W}\right) \approx \frac{\delta_{\mathrm{PS,SS}}}{\delta_{h,s}}\left(\frac{\Delta\beta}{\Delta\sigma} + \frac{1}{\mathrm{Ro}}\right) \tag{9}$$

where $\Delta\beta$ is the overall turning from the impeller inlet to the exit, $\Delta\sigma$ the flow turning angle in the meridional surface, and $\mathrm{Ro} = W/\omega R_m$ the Rossby number. It can be seen from Equation (9) that the balance of the blade surface vortices and the passage vortices depends on the ratio of the streamline curvatures in the blade-to-blade and meridional surfaces, the Rossby number and the ratio of the boundary layer thicknesses of the endwalls and the blade surfaces. The ratio of the boundary layer thicknesses could be close to one for most of the practically used machines. Hence the important contributions are from the impeller geometry and the Rossby number. Reducing the overall turning angle, such as applying backsweep to the blade profile, the endwall passage vortices will become less important, resulting in the wake position being shifted away from the shroud/SS corner towards the pressure side, as seen from Figure 2.

For a given impeller, its discharge flow profile will depend on its rotational speed and the flow rate, that is, the Rossby number. The influence of the Rossby number on the wake location has been reported by Johnson and Moore [20]. They found, from their experimental studies in a shrouded impeller with radial discharge, that the wake is located on the suction surface in the 'below design' flow, near the shroud/SS corner in the 'design flow' and on the shroud in the 'above design' flow. This is due to the progressively dominating effect of the BV on the (PV + CV) when mass flow is increased.

In addition, contributions of tip leakage flow to the wake position are not included in Equation (9). In an unshrouded impeller, the tip leakage flow acts in a direction opposite to the shroud passage vortex and tends to move the endwall fluid from the shroud/SS corner

towards the pressure side. As discussed in [26, 22], Equation (9) deduced for a shrouded impeller, holds also for an impeller with tip clearance.

3. Brief description of the LSCC

The LSCC (Low Speed Centrifugal Compressor) is an experimental facility designed to duplicate the essential flow physics of high-speed subsonic centrifugal compressor flow fields in a large size, low-speed machine. A complete description of the facility can be found in [30].

The compressor has a backswept impeller, followed by a vaneless diffuser. The impeller has 20 full blades with a backsweep of 55°. The inlet diameter is 0.870 m and the inlet blade height is 0.218 m. The exit diameter is 1.524 m and exit blade height is 0.141 m. The tip clearance between the blade tip and the shroud is 2.54 mm, and is constant from the impeller inlet to exit. The design tip speed is 153 m/s, with a rotation speed of 1862 rpm and a design mass flow of 30 kg/s. The experimental measurements include static pressures on blade surfaces and shroud wall, velocity components with laser anemometer at 18 cross-sections from the upstream to downstream of the impeller.

4. Numerical calculation method

In all computations, the Navier-Stokes code EURANUS integrated in the Fine/Turbo interface by NUMECA International, was used. This software, already presented in [31], solves the time-dependent Reynolds averaged Navier-Stokes equations, with either the algebraic turbulence model of Baldwin-Lomax or a two-equation k-ε model for closure. It is based on a structured multiblock, multigrid approach, including non-matching block boundaries and incorporates various numerical schemes, based on either a central or an upwind discretization.

For the present calculations, the linear k-ε model of Yang and Shih [32], modified by Khodak and Hirsch [33], is selected, in which the damped function used in the eddy viscosity is chosen to be a function of $R_y = (k^{1/2} y/v)$. For comparison, computations with the algebraic turbulence model of Baldwin-Lomax were also done. The calculations were performed with a second-order centered scheme, with second and fourth order artificial dissipation terms and a W-cycle multigrid technique. The numerical procedure applied a four-stage Runge-Kutta scheme, coupled to local time stepping and implicit residual smoothing for convergence acceleration.

4.1. Computational grid

A grid with three blocks, obtained with the auto-grid generation software IGG/Auto-Grid of NUMECA, is used in this study. The first block covers the flow passage, extended from 40% meridional shroud length upstream of the impeller, to 15% impeller tip radius downstream in the radial direction. The second block represents the region behind the blunt trailing edge. The third block occupies the space in the tip gap. A blunt blade tip is meshed, even though the real tested blade tips are rounded as reported by Chriss *et al.* [21]. The mesh consists of $61 \times 73 \times 129$, $13 \times 73 \times 33$ and $13 \times 13 \times 65$ points, in the tangential, radial and streamwise directions, for blocks 1, 2 and 3, respectively. Hence there are 13 lines over the gap height and 13 lines across the blade profile. This mesh is named as the Basic Mesh. To investigate the mesh dependence, two other meshes, Coarse Mesh and Fine Mesh listed in Table 1, were also computed.

Table 1. Grid characteristics

	Block 1	Block 2	Block 3	Total points
Basic Mesh	61×73×129	13×73×33	13×13×65	616739
Coarse Mesh	49×61×129	13×61×33	13×13×65	422735
Fine Mesh	73×97×129	25×97×33	25×25×65	1034099

Particular care has been taken in order to ensure sufficient resolution in the endwall and blade boundary layers by controlling the position of the mesh points close to the solid surfaces. The grid location near the blade surfaces produces Y-plus for the first cell center being about 1.

4.2. Boundary conditions

At the inlet plane, measured profiles of absolute flow angles and total pressure, uniform total temperature, turbulent kinetic energy k and dissipation ε are imposed. As in the experiments, the hub wall of the impeller is moving with the rotor blade, while the diffuser hub is stationary. The whole shroud is stationary. All the solid wall boundaries are assumed to be adiabatic. Periodic conditions are enforced along the boundaries upstream and downstream of the impeller, and also in the gap.

4.3. Convergence

The computations are performed at a CFL number of 2.5 and are converged to near machine accuracy, that is 4 to 5 orders of residual reduction and constancy of mass flow. The error in mass flow between inlet and outlet of the computational domain is less than 0.1%.

5. Validation and discussions

5.1. Overall performance

To investigate the variations of the 3D flow within the centrifugal impeller blade channel with flow rate, the computations were performed over a mass flow range as wide as possible. Considering the available experimental data, three mass flow rates, 23.6kg/s (partial flow), 30kg/s (design flow), and 39.7kg/s (high flow) were selected. For the partial and design flow rates, 3D data in the flow channel and on the blade surfaces and the 2D data behind the impeller exit are available. The high flow condition is the highest flow rate for which the experimental data of shroud static pressure is available.

Computations with the linear k-ε model and the Basic Mesh have been done for all the three flow conditions. Figure 5 shows the comparison of overall performance with experimental data, in which the CFD data were mass-averaged over the grid points, at 6.7% impeller tip radius downstream of the impeller exit. It is seen that the pressure ratio is in excellent agreement with the data at all the computed flow rates. The efficiencies are over-predicted by about 2%. The discrepancy in efficiency may be related to the under-prediction of total temperature ratio, see below for details.

Computations with the Coarse Mesh were carried out for both design and partial flow conditions, while the computation with the Fine Mesh was only performed at the design flow rate. For the pressure ratio, the prediction with the coarse mesh is about 0.2% lower than with the other meshes, while the difference in the predicted efficiency falls in a band of 1.5%. Computations with the Baldwin-Lomax model and the Basic Mesh, were

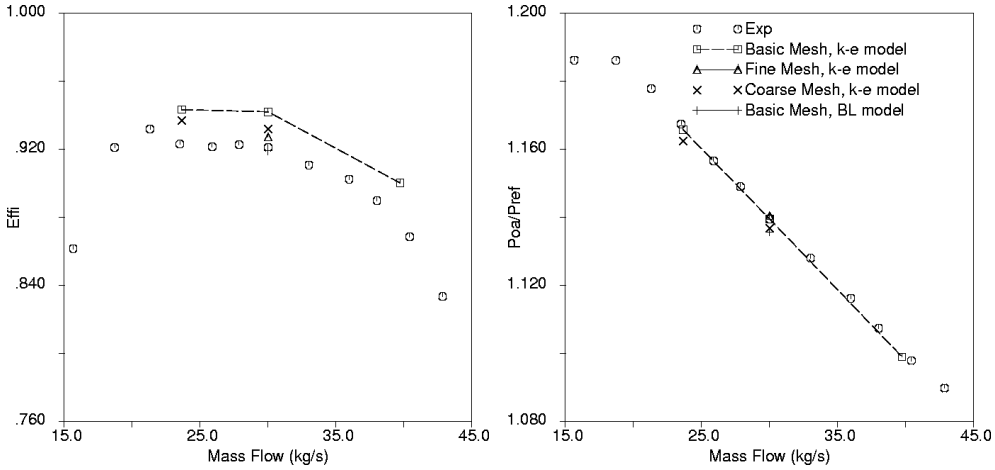

Figure 5. Overall performance

also performed at the design flow rate condition. Compared to the k-ε model, no apparent difference is visible in the pressure ratio, but about 1% lower in the efficiency.

5.2. Pitch-averaged profiles behind impeller exit

Shown in Figure 6 are the pitch-averaged numerical results of static pressure, absolute total pressure and temperature, and absolute flow angles at Station 2 for the three flow rates. Station 2, as named by Hathaway *et al.* [30], is located in the vaneless diffuser, at 6.7% impeller tip radius downstream of the impeller exit. The computations were done with the Basic Mesh and linear k-ε turbulence model (hereafter, if there is no specific indication, all computations were performed with the Basic Mesh and linear k-ε turbulence model). Experimental data in partial and design flow conditions, which are available, are included. As seen from Figure 6, all computed data are globally in agreement with the experiments for both design and partial flow conditions, except for the flow angles near the hub (with large Z). The flow angle discrepancy near the hub is due to the over-prediction of the pressure surface vortex, BVP, which will be further discussed in connection with Figure 17. The total temperature ratio is under-predicted over a wide range, which may be associated with the over-predicted efficiency (Figure 5). The static pressure is nearly constant from hub to shroud in all three conditions.

5.3. Static pressure distribution

Figure 7 compares the static pressure along the shroud for the design, partial and high flow conditions. Excellent agreement is noticed for all flow conditions over the whole measured range. It is noted that the distribution of static pressure at the different flow rate conditions is essentially the same over a wide range of the flow passage. At the impeller inlet region, the static pressure shows a moderate positive gradient at the partial flow condition, compared to the intense negative gradient at the high flow condition. The same observation was also made by Hah *et al.* [34] in their CFD simulation of the 3D flow in the high subsonic flow impeller of [7]. The negative gradient at the high flow condition is associated with a high negative incidence, which can be seen from Figure 8 and discussed in the following paragraph.

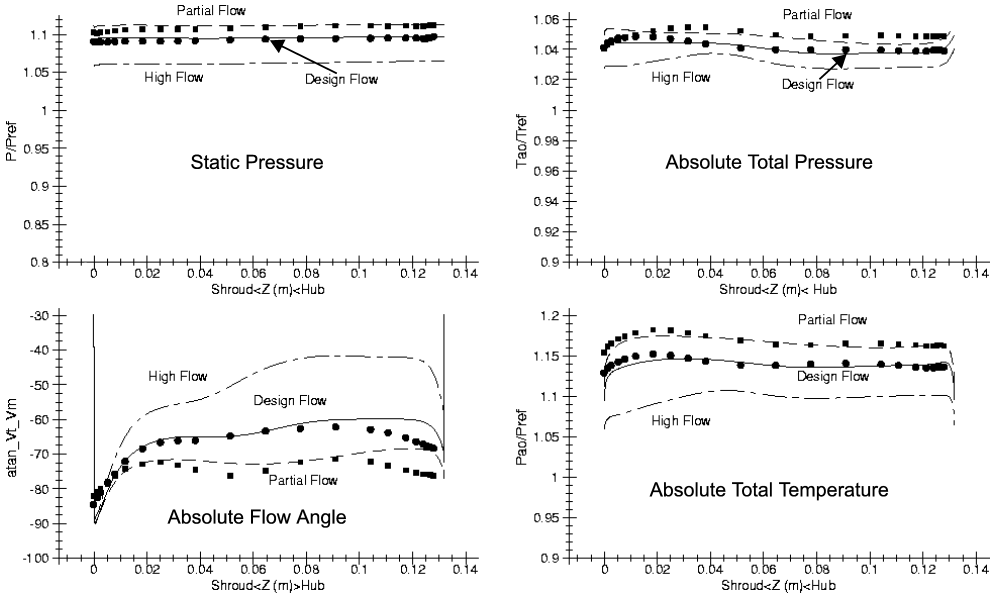

Figure 6. Comparison of pitch-averaged profile behind the impeller exit: linear k-ε model and Basic Mesh Partial flow rate – – – CFD, ■ experiment; Design flow rate —— CFD, ● experiment; High flow rate — · — CFD

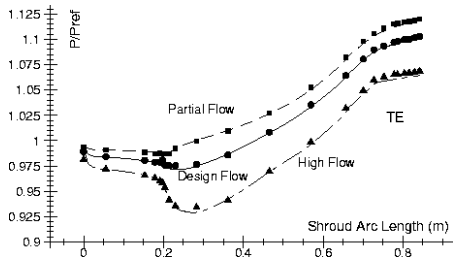

Figure 7. Comparisons of shroud static pressure, linear k-ε model and Basic Mesh: Partial flow rate – – – CFD, ■ experiment; Design flow rate —— CFD, ● experiment; High flow rate — · — CFD, ▲ experiment

Quantitative comparions of reduced static pressures on the blade surfaces at all measured spanwise sections from 5% to 98% span are presented in Figure 8, for the three mass flow conditions. Figures 9 to 11 present their isolines from which the global features of the flow fields can be viewed. The reduced static pressure is defined as in [14]:

$$\mathrm{Pr} = P \Big/ \left[\left(T^* + \frac{\omega^2 r^2}{2C_p} \right) \Big/ T^* \right]^{\frac{\gamma}{\gamma - 1}} \tag{10}$$

where $T^* = T + (W^2 - \omega^2 r^2)/2C_p$.

As seen from Figures 8 to 10, excellent agreement is achieved over a wide range of the blade surfaces for both the partial and design flow conditions. It seems that the flow incidence at the partial flow condition is over-predicted, as the predicted pressures close to the impeller inlet in both pressure and suction surfaces are higher than the data (Figure 8). At the high flow condition, the loading is negative near the leading edge and

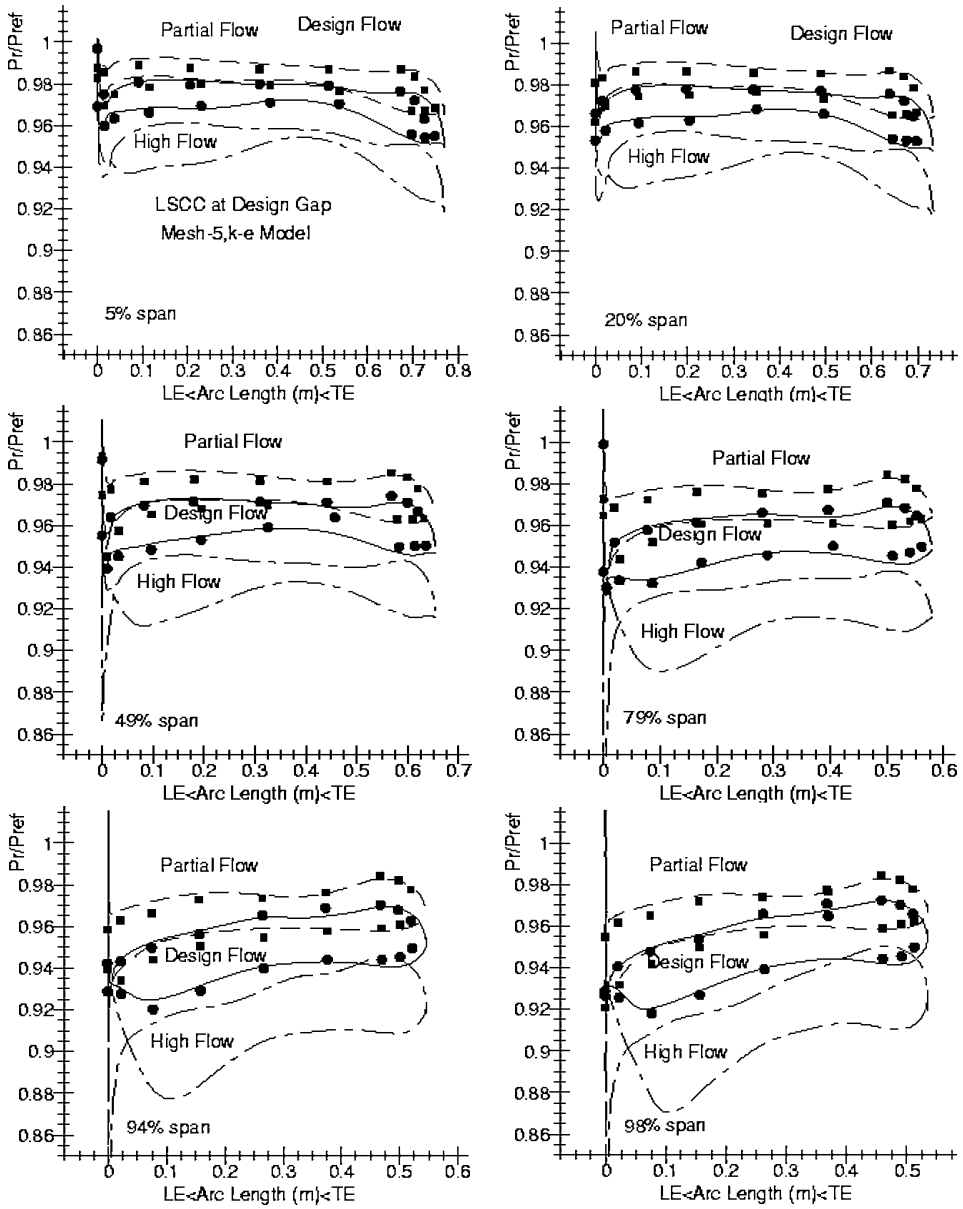

Figure 8. Comparisons of reduced static pressure distributions at spanwise sections: Partial flow rate – – – CFD, ■ experiment.; Design flow rate —— CFD, ● experiment; High flow rate — · — CFD

reduces towards the tip. This negative loading reveals the negative operating incidence, which results in the pressure drop as observed in Figure 7. It can also be noticed, from the remaining streamwise region, that the local blade loading is increasing with the spanwise distance, and with flow rate as well. The latter indicates that in the centrifugal impeller, increasing the overall pressure rise with reducing the flow rate results in a reduction in the blade pressure loading. This can easily be understood from the tangential momentum equation as in [21].

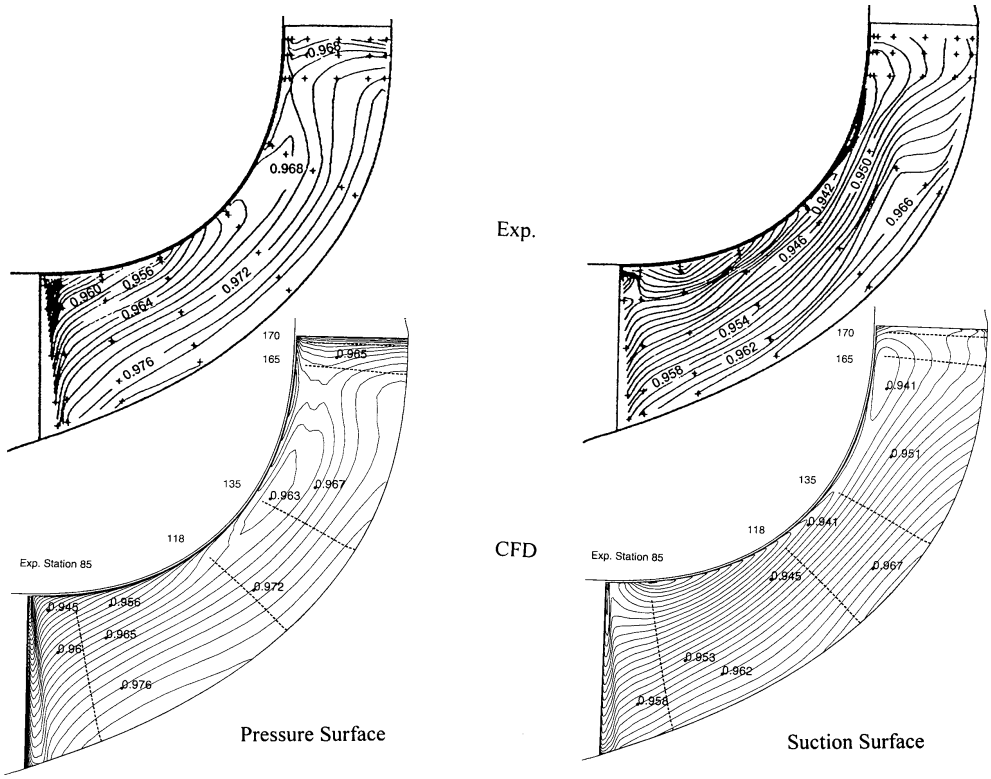

Figure 9. Isolines of reduced static pressure on blade surfaces, at design flow rate, linear k-ε model and Basic Mesh

As seen from both numerical and experimental data in Figures 8 to 11, a pressure gradient pointing from the hub to the tip, due to the wall curvature, is present in almost the whole channel from the inlet to exit, for all three flow rates. It decreases in the streamwise direction and reaches a uniform distribution near the exit as described by Equation (2). As the intervals of the isolines for all plots in Figures 9 to 11 are constant, 0.002, the isoline density is indicative of the pressure gradient strength. It is then observed that: i) the pressure gradient for a given flow rate is higher on the suction surface than on the pressure surface; ii) the maximum gradient is located in the inducer part (from the impeller inlet to station 85, approximately) and shifts towards the leading edge with the increasing mass flow; and iii) the gradient increases with the mass flow. This pressure gradient, together with the centrifugal force, will drive the low energy fluid inside the blade surface boundary layers from the hub towards the shroud and re-enforce the development of the blade surface vortex BVS and BVP in Figure 3. It can then be expected that the strength of the blade surface vortex BV will increase with the flow rate. In addition, the isoline loops on the pressure surface are associated with the impinging of the tip leakage flow and shifting downstream with the increasing flow rate. Details of the tip leakage flow will be discussed later.

5.4. Flow near blade surface

Figure 12 shows comparisons of flow traces near the pressure and suction surfaces for the design flow. For the partial and high flow rates, only the results near the pressure surface

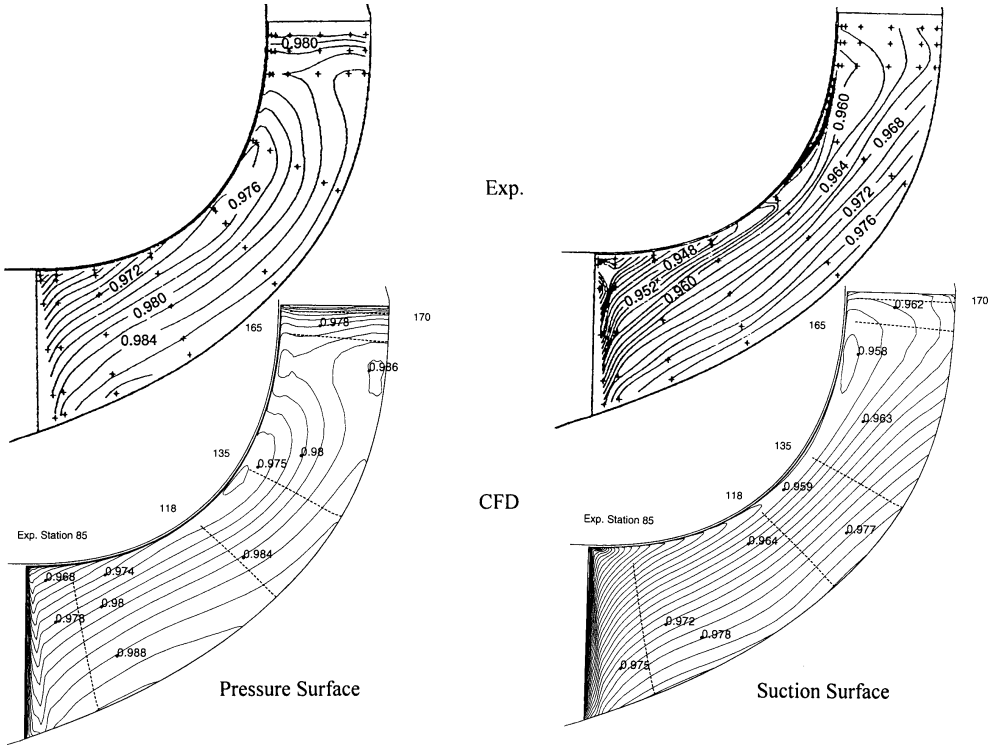

Figure 10. Isolines of reduced static pressure on blade surfaces, at partial flow rate, linear k-ε model and Basic Mesh

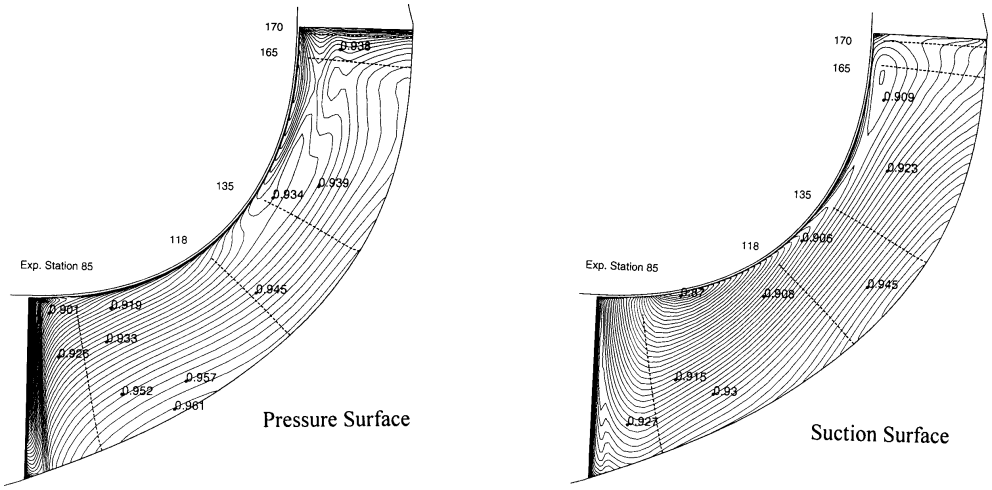

Figure 11. Calculated isolines of reduced static pressure on blade surfaces at high flow rate, linear k-ε model and Basic Mesh

are presented in Figure 13 as the flow near the suction surface has a similar behaviour for different flow rates. The CFD results show the velocity vectors, on the second mesh surface, at each second grid point for reasons of clarity.

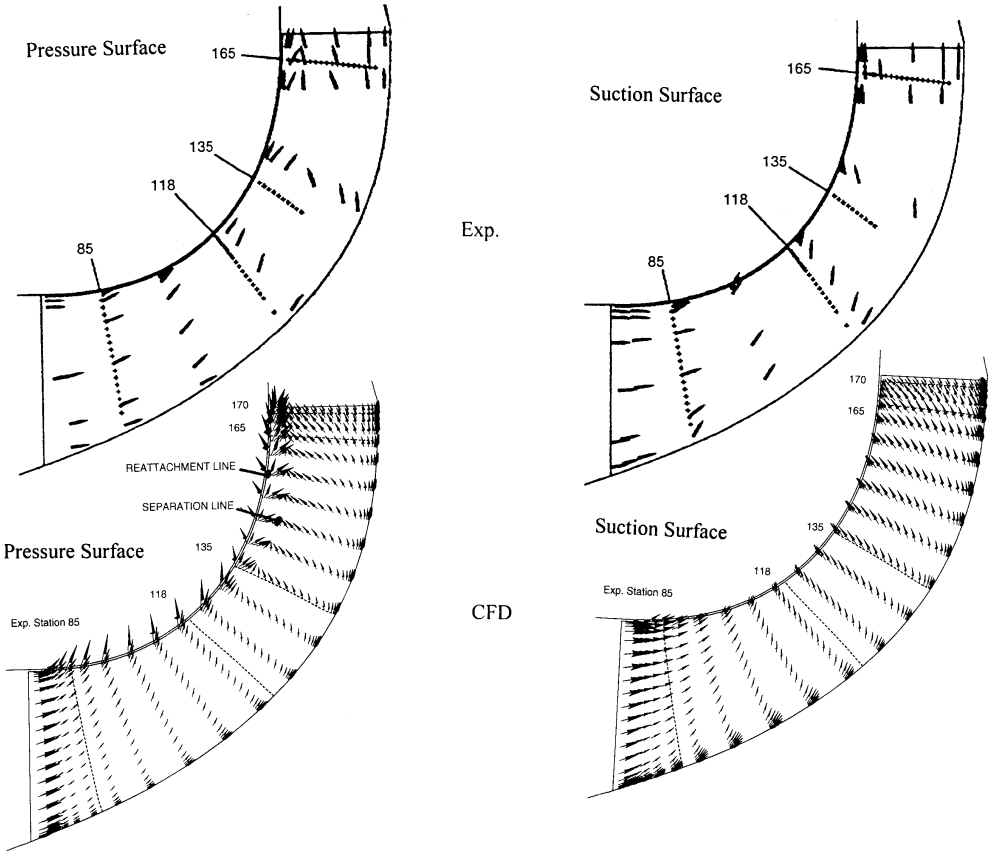

Figure 12. Comparison of velocity vectors near the blade surfaces at design flow rate, linear k-ε model and Basic Mesh

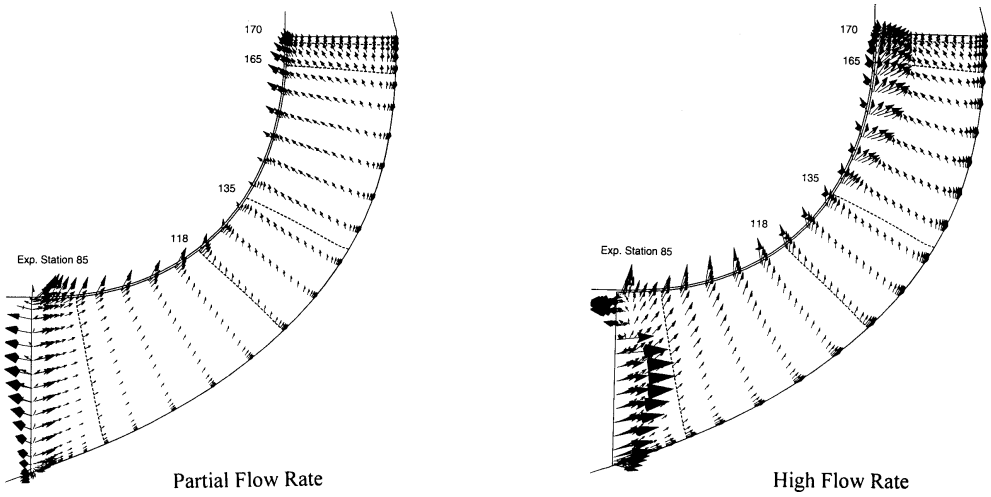

Figure 13. Calculated velocity vectors near pressure surface for partial and high flow rates, linear k-ε model and Basic Mesh

Due to the pressure gradient observed in Figures 9 to 11, the flow near the blade surface migrates from hub to shroud over a wide range. The strength of the transportation can be read approximately from the velocity vector inclinations away from the mainstream direction which can be assumed along the wall boundaries. This transport is well simulated, except close to the trailing edge in which an over-prediction is noted. It can be observed from Figures 12 and 13, as expected, that: i) the secondary flow is stronger on the suction surface than on the pressure surface in the first half portion of the flow channel; ii) with the increasing mass flow the inclination becomes stronger. Contrary to the reduction of the pressure gradient from the inlet to the exit, as seen from Figures 9 to 11, the transportation of boundary layer fluid along the blade increases with the streamwise distance. These observations imply that the spanwise migration in the first half of the channel, from the inlet to station 118, is mainly driven by the pressure gradient, while in the remaining part the migration is not only due to the pressure gradient but also due to the inertia of the secondary flows well developed in the first half portion of the channel.

The most interesting flow phenomena in Figures 12 and 13 are separation and reattachment lines near the blade tip in the pressure side for both design and high flow rates. The separation line has its origin nearby station 135 in both cases. The separation region decreases with the mass flow and disappears at the partial flow condition. This flow separation is related to the impinging of the tip leakage flow on the pressure surface and will further be discussed later. In addition, due to the high negative incidence for the high flow rate, the flow in the inlet tip region (Figure 13) is separated.

5.5. Throughflow development

Figure 14 shows comparisons of the computed throughflow isolines with the experimental results at stations 85, 118, 135, and 165, as indicated. The throughflow velocity is normalised with the exit tip speed. It is seen from Figure 14 that the predicted throughflow velocity compares globally well with the experiments in all the measured stations. Near the impeller inlet, at station 85, the region with condensed isolines in the shroud/SS corner in the CFD results is associated with the tip leading edge vortex, which can not be seen in the experimental results due to its small size. At stations 118 and 135, between which the flow channel transits from the axial to radial direction, the throughflow wake is clearly seen as the condensed isoline pattern in the shroud/PS corner from both CFD and experimental results. This region tends to increase from station 118 to 135, which is well captured by the computations. In the radial portion of the flow passage, station 165, this low energy wake region has migrated towards the mid-pitch near the shroud, as a result of the growing shroud CV, Coriolis vortex. The Coriolis vortex is believed to be much stronger in the shroud side, due to the thicker boundary layer, than that in the hub side.

As a comparison, the CFD results, computed with the Coarse and Fine meshes, are also presented in Figure 14 for stations 135 and 165. It is seen that significant differences can be observed between the different meshes, in particular along the suction surface whose boundary layer thickness is mesh sensitive. The computations with coarser meshes show a larger low energy fluid region near both blade surfaces and the shroud, and curvature of the isolines around the channel center is slightly stronger. It is observed from the CFD plots that the blade surface boundary layer thickness is over-predicted, which may cause the strong curvature of the isolines in the channel center region.

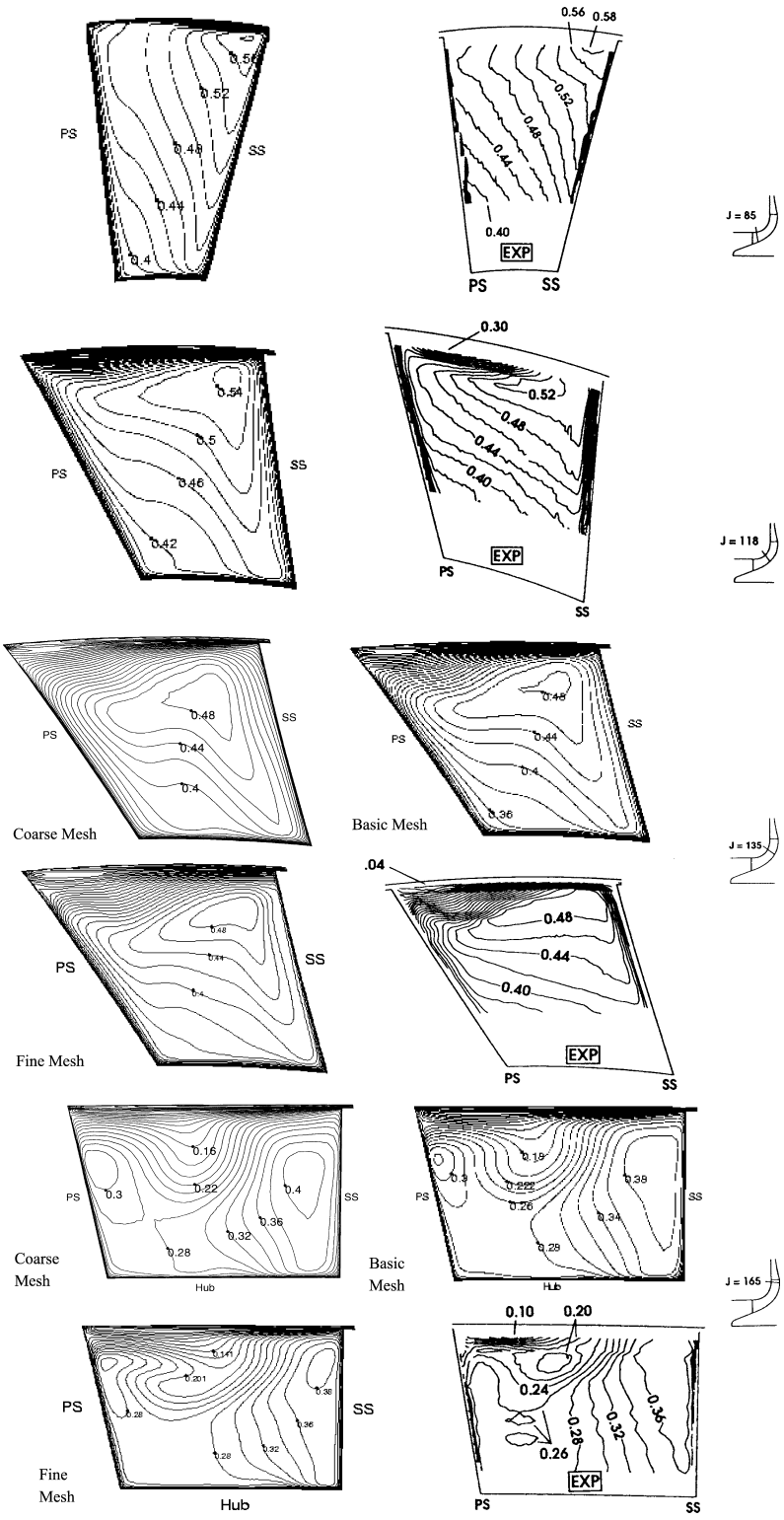

Figure 14. Isolines of throughflow velocity at design flow condition, linear k-ε model

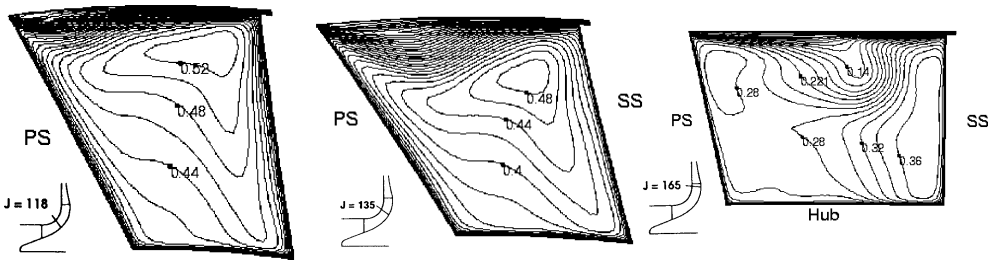

Figure 15. Isolines of throughflow velocity at design flow condition, Baldwin-Lomax model and Basic Mesh

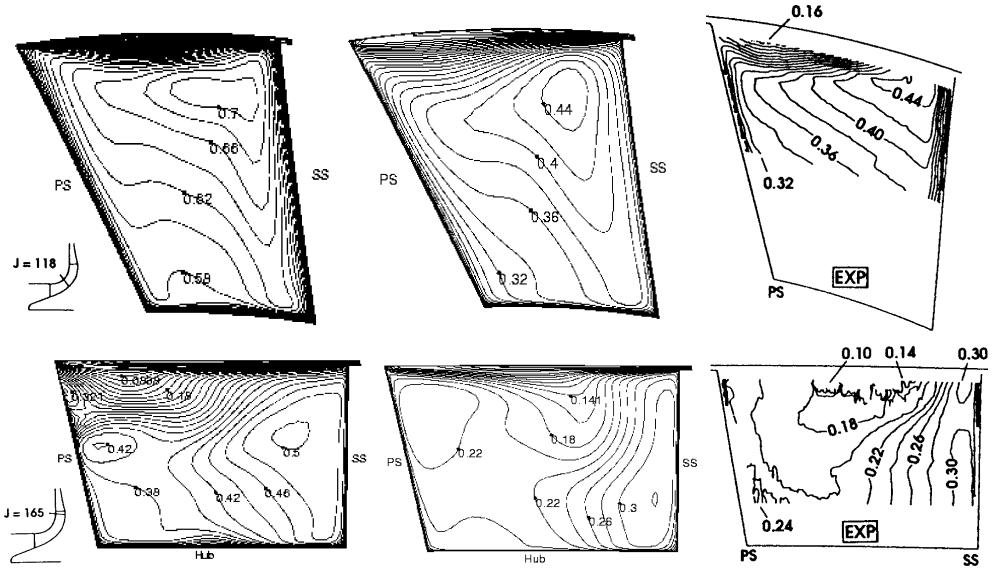

High low Partial flow Partial flow

Figure 16. Isolines of meridional velocity at off-design conditions, CFD: linear k-ε model and Basic Mesh

Figure 15 presents the isolines of meridional velocity at stations 135 and 165, computed with Baldwin-Lomax turbulent model and the Basic Mesh. The computations with Baldwin-Lomax turbulent model are globally consistent with those of the linear k-ε model. However, a difference exists in the flow details. Compared to the experimental and CFD results in Figure 14, one can see the wake region is closer to the suction side in the simulation with the Baldwin-Lomax turbulent model. It has been known that the location of the wake (low velocity area) in a centrifugal impeller is determined by the balance of all the secondary flow resources, as discussed earlier. This may indicate that the computation with the Baldwin-Lomax turbulent model under-predicts the tip leakage flow but over-predicts the Coriolis vortex.

Figure 16 presents the isolines of computed throughflow velocity, for partial and high flow rates, at stations 118 and 165, with experimental data for the partial one. It can be seen that the predicted throughflow velocities at the partial flow rate compare globally well with the experiments. The throughflow wake observed in Figure 16 is an accumulation of the fluid with a low throughflow velocity. It is observed that the center of the wake at Station

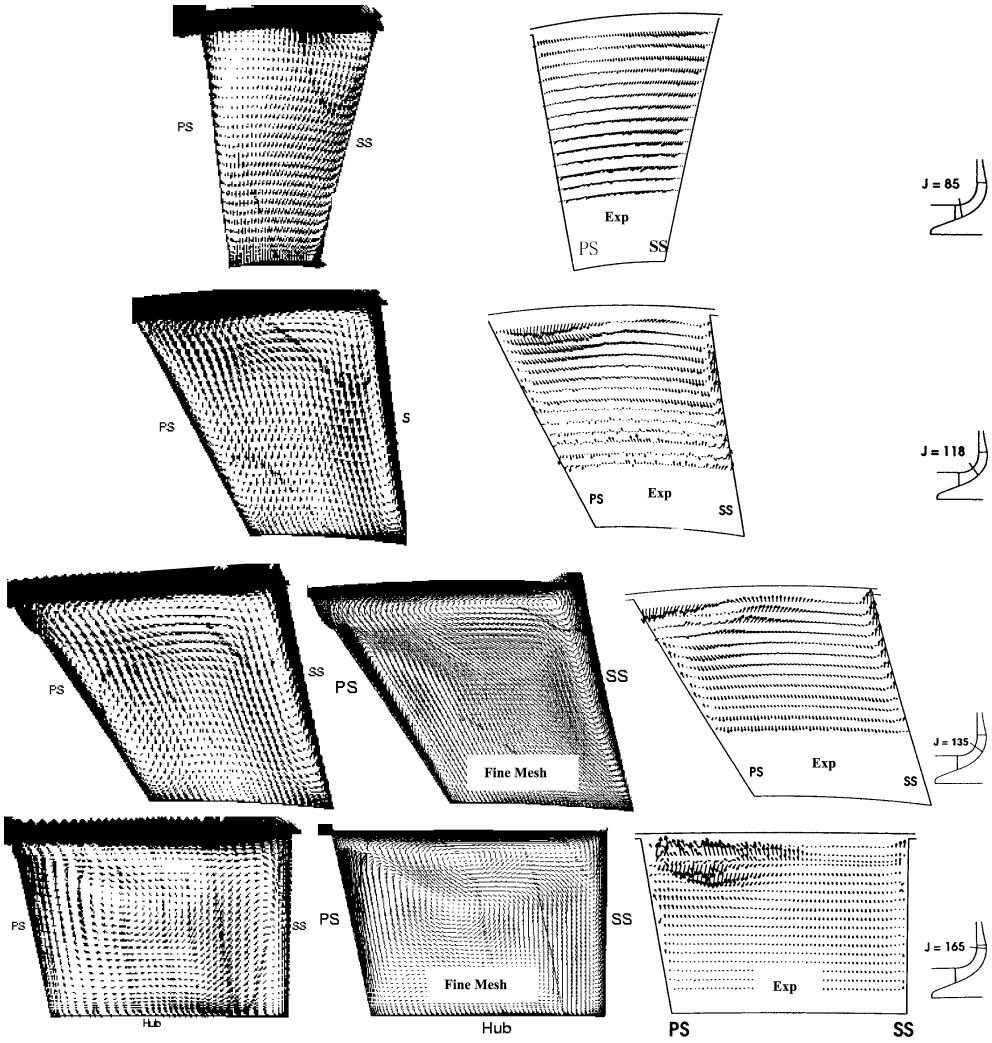

Figure 17. Secondary velocity vectors at different streamwise station at design flow rate, computed with linear k-ε model and Basic Mesh

165 is located in the suction side of the mid-pitch of the station at the partial flow case. The wake is then shifting towards the shroud/PS corner with the increasing flow rate as described by Equation (9). At station 118, however, the wake is closer to the SS for the low flow rate than that for the high flow rate. This is because the low velocity region in front of station 135 is mainly attributed to the tip leakage flow and tip leakage vortex. The vortex core shifts towards the suction side with the increasing flow rate. See more details later.

Secondary Flow Development Figure 17 shows comparison of the computed secondary velocity vectors with the experimental ones at stations 85, 118, 135, and 165. The secondary velocity vectors are defined by their components perpendicular to the streamwise oriented mesh lines as the mesh is body-fitted. As discussed earlier, the main mechanism for the accumulation of the low energy fluid in the shroud area is due to the radial transport of the boundary layer material along the blade surfaces and its location results from a balance between the passage vortices (PVH, PVS and CV), blade surface vortices (BVS and BVP)

and tip leakage flow. All these vortices can also be seen from both CFD and experimental plots in Figure 17. However, differences between the CFD results and the experimental ones are obvious. It is seen in stations 118 and 135 that the sizes of the computed BVP and BVS are larger than those of the experiments, which is related to the over-predicted boundary layer thickness as seen from Figure 14. The second difference exists in the shroud/PS corner in station 135. In the experiment, a well-behaved vortex is observed in the shroud/PS corner. It is the tip leakage vortex and has its origin at the tip leading edge. Downstream of station 135, this vortex tends to move away from the corner towards the channel center, driven by the pressure surface vortex BVP. It seems that the diffusion of the predicted vortex is much faster than in the experiments, which may be connected to the fact that the computational results are still mesh dependent. The third difference lies in the shroud/PS corner in station 165. In the experiment, the most dominant flow feature is the strong flow reversal of the spanwise flow direction in the corner. This reversal of flow direction, coupled to an observed high level of velocity fluctuations was explained as local flow unsteadiness by Chriss *et al.* [21]. From the CFD results, this observed unsteadiness might be connected to the high shear region where strong interactions exist between the two oppositely moving flows, the tip leakage flow and the flow induced by BVP. Another difference in station 165 is the vortex motion near the channel center in the CFD plot but not in the experiment. This vortex is the pressure surface vortex, BVP. Due to its strong motion, a short distance above the hub wall, the flow transports from the suction to the pressure side, which explains the over-predicted flow angle in Figure 6.

6. 3D flow structure in flow passage

Figure 18 shows 3D configuration of the streamlines, issued from the blade leading edge, at the design flow condition. The suction surface in this plot is made transparent. Contours of through-flow velocity at mesh surfaces nearby the stations 85, 118, 135, and 170 are also presented. The red lines are the trajectories of particles released from the

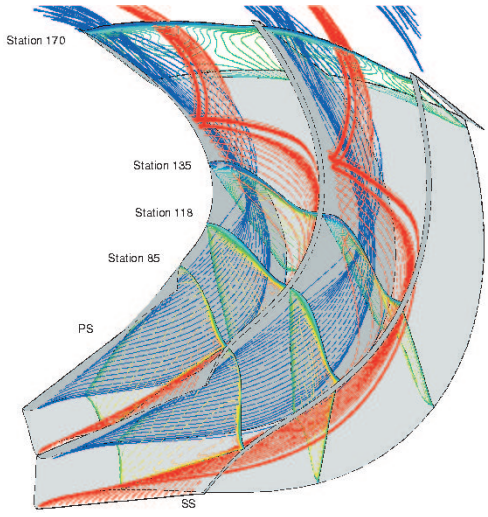

Figure 18. 3D streamlines released from the blade leading edge:
red lines from suction side and blue lines from the pressure side, at design flow condition
and computed with linear k-ε model and Basic Mesh

suction side leading edge a short distance away from the hub and shroud, while the blue lines are released from the pressure side leading edge. As already observed, all the red lines in the inducer portion migrate upward towards the shroud along the suction surface. Lines close to the shroud move away from the suction side towards the pressure side just behind station 118 and reach the mid-pitch region at Station 135. The remaining lines concentrate and migrate into the shroud/SS corner behind Station 135, associated with the BVS motion. They are then tangentially transported away from the corner towards the mid-passage pushed by the tip leakage flow, see the next section for details of the tip flow. These streamlines then turn back downward towards the hub in the shroud/PS corner, due to the combined effect of the BVP and CV. All these streamlines leave the impeller in the through-flow wake region at station 170. The blue lines along the pressure surface move also upwards from hub to shroud in the inducer portion. The vortex motion associated with the BVP can be observed in front of station 118 in the shroud/PS corner, in Figure 18, from which streamlines near the shroud leave away from the pressure surface. Other lines remain close to the surface up to station 135. Behind this station, these lines move spirally downstream under the red lines, by the effect of a strong BVP. They also pass through the through-flow wake range in station 170.

7. Tip leakage flow structure

The flow phenomena in the blade tip region are illustrated in Figures 19 and 20, which show, respectively, isolines of static pressure on the shroud, and 3D streamlines generated in the tip gap, in two flow passages, for the three flow rates. The pressure troughs in Figure 18 reveal the evolution of the tip leakage vortex, which is marked by the dashed lines. As a comparison, pressure isolines on the shroud without a tip gap are also presented in Figure 19. It can be seen that at low flow conditions, the tip leakage vortex is more inclined to the tangential direction than for high flow conditions, due to the increase of blade loading (Figure 7). Increasing of the blade loading from the partial to design flow rate results in increasing of the overall tip leakage flow from 7.97% to 8.49% of the impeller design mass flow. However, due to the high negative incidence in the high flow condition, the overall tip leakage flow (from PS to SS) is only 7.82%, even though the local leakage flow over a wide range in the chordwise direction is increased. The negative tip leakage flow (from SS to PS) at high flow condition can also be realised from the 3D streamline view in Figure 20 and is discussed below.

The red lines in Figure 19 are released from a small region in the tip gap at the leading edge. The blue lines are issued from the tip gap around station 118. The pink lines are issued in the tip gap near station 135. At both partial and design flows, a tip leakage vortex presented by the red and blue lines in Figure 20, passes through station 85 in the shroud/SS corner, which has also been seen from the computed secondary velocity vector plot in Figure 17 but not from the experiments since its size is very small at this station. The tip vortex sweeps tangentially over the blade passage and reaches the shroud/PS corner in front of station 118 for partial flow and behind station 118 for design flow. Further downstream, the vortex core shifts away from the corner, due to the transverse pressure gradient, which causes the formation of isoline loops of pressure on the pressure surface (Figures 9 and 10). It then remains in the low throughflow range up to the impeller exit. At high flow conditions, the red lines move into the other blade passage due to the negative

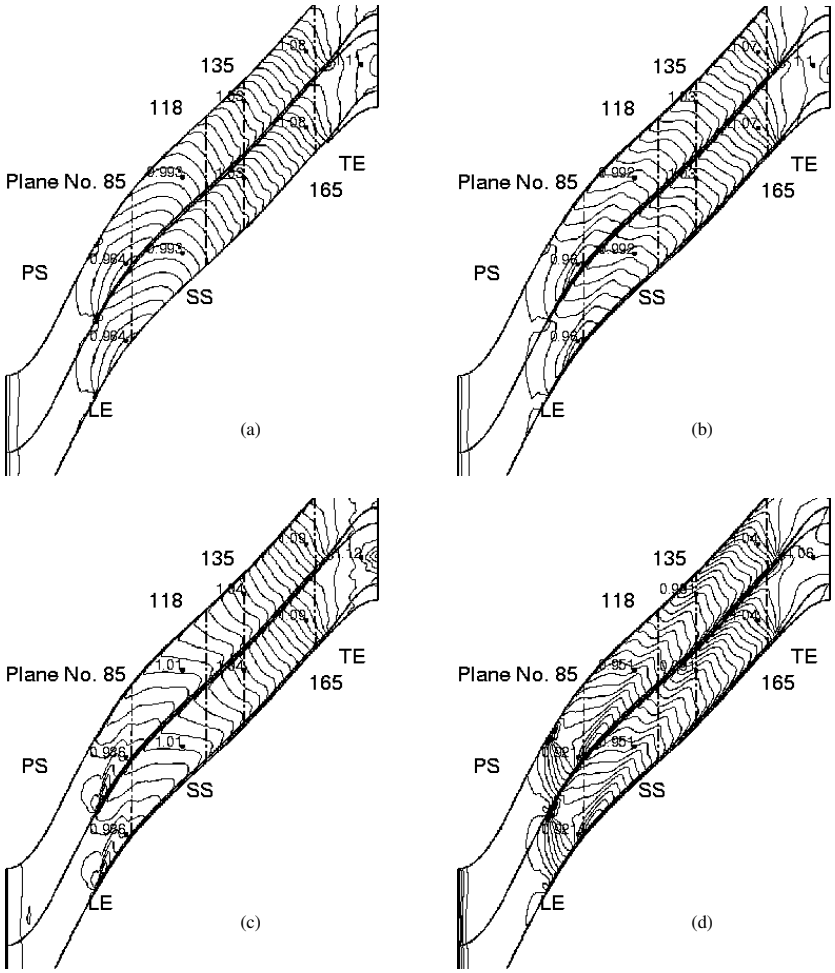

Figure 19. Isolines of static pressure on shroud: (a) no gap at design flow, (b) design flow, (c) partial flow, and (d) high flow, computed with linear k-ε model and Basic Mesh

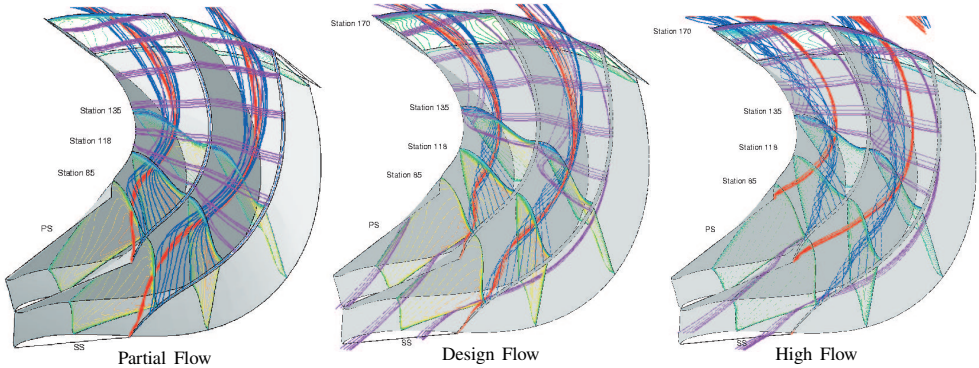

Figure 20. 3D streamlines released from different regions in the tip gap: red lines from the leading edge; blue lines from between the leading edge and midchord; and pink likes from downstream of the midchord, at different flow conditions, computed with linear k-ε model and Basic Mesh

loading in the leading edge portion (Figure 8), resulting in the negative tip leakage flow. The blue lines form the tip leakage vortex, which is originated just upstream of station 85 and is located closer to the suction surface than for the lower flow conditions, as seen from Figure 19. The blue lines move towards the pressure side along the shroud up to station 135, where it contributes to the low energy region in the shroud/PS corner. From this station to the exit, they remain near the red lines. The pink lines at all three flow conditions are issued in the tip gap near station 135. In the radial portion of the flow passage, behind station 135, they move away from the suction surface towards the shroud/PS corner. From the shroud/PS corner in front of station 135 for lower flow rates and behind this station for higher flow rate, they move downstream rejoining the red and blue lines. All lines released from different chordwise locations leave out the impeller from the low velocity region.

It can then be stated that first signs of the wake are observed, with very small size, from the shroud/SS corner. In the first half of the blade passage, the wake is mainly attributed to the tip leakage flow and tip leakage vortex. Its location shifts towards the suction side with the increasing flow rate. Hence the wake moves away from the pressure side with the increasing flow rate (Figures 14 and 16). In the midway of the blade passage, around station 135, low energy fluids from the blade surfaces, associated with the blade surface vortices (BVp and BVs) (Figure 17), and from the tip leakage have merged together, resulting in a large size of the wake region in the pressure/shroud corner. In the remaining blade passage, the radial portion, the secondary flow is dominated by the contribution of the Coriolis force, which is inversely proportional to the meridional velocity. It results in the wake approaching to the suction side with the decreasing flow rate.

8. Conclusions

The 3D viscous flow in centrifugal compressor impellers has been investigated theoretically and numerically. The analysis gives an insight into basic mechanisms leading to the formation of the jet/wake flow structure in centrifugal machines. The main mechanism for the accumulation of low energy fluid in the shroud area is the radial transport of boundary layer material along the passage surfaces. Its location results from a balance between the shroud passage vortex, blade surface vortices and tip leakage flows. The balance depends on the ratio of streamline curvature in the blade-to-blade and meridional surfaces, the Rossby number and the ratio of the boundary layer thickness the endwalls and blade surfaces.

The Large Scale Centrifugal Compressor (LSCC) impeller with a vaneless diffuser has been investigated at three flow rate conditions with EURANUS/TURBO with different meshes and turbulence models. An excellent agreement with the available experimental data has been obtained over a wide region of the flow passage. A grid at order of 600 000 points was required to get the overall performance, while more points are needed to scrutinise the flow details. To reproduce some micro flow phenomena, unsteady flow computation was necessary.

Structures of the 3D flow in the blade passage and the tip region, and their variations with flow rate as well, were analysed based on the numerical results. The tip vortex originating at the tip leading edge sweeps tangentially over the blade passage and reaches the shroud/PS corner near the midchord. Further downstream, the vortex core shifts away from the corner and remains in the low throughflow area up to the impeller exit. In the first half of the blade passage, the low energy fluid area is mainly attributed to the core of

the tip leakage vortex. Its location shifts towards the suction side with the increasing flow rate. In the midway of the blade passage, the low energy fluids from the blade surfaces and the tip leakage have merged together, resulting in a large size of the wake region in the pressure/shroud corner. In the remaining blade passage, the radial portion, the secondary flow is dominated by the Coriolis force, resulting in the wake approaching the suction side with the decreasing flow rate.

References

[1] Langston L S, Nice M L and Hopper R M 1977 *J. of Engineering for Power* **99** 21

[2] Chen T G and Goldstein R J 1991 *J. of Turbomachinery* **114** (4) 776

[3] Schulz H D, Gallus H E and Lakshminarayana B 1990 *J. of Turbomachinery* **112** 669

[4] Cumpsty N A 1989 *Compressor Aerodynamics* Longman Scientific and Technical, Essex, England

[5] Kang S and Hirsch Ch 1995 *J. of Turbomachniery* **118** 492

[6] Kang S 1993 *Investigation on the Three-Dimensional Flow Within a Compressor Cascade with and without Tip Clearance* PhD Thesis, Dept. of Fluid Mech., Vrije Universiteit Brussels

[7] Eckardt D 1979 *Flow Field Analysis of Radial and Bachswept Centrifugal Compressor Impellers, Part 1: Flow Measurements Using Laser Velocimeter* Performance Prediction of Centrifugal Pumps and Compressors, Gopalakrishnan, ed. ASME Publication, pp. 77–86

[8] Dean R C and Senoo Y 1960 *Trans. ASME, Journal of Basic Engineering* **82** 563

[9] Dean R 1971 *On the Unresolved Fluid Dynamics of the Centrifugal Compressor* in Advanced Centrifugal Compressors, ASME Publications pp. 1–55

[10] Eckardt D 1976 *J. of Fluids Engineering* **98** 390

[11] Moore J 1973 *J. of Eng. Power* **95** 205

[12] Johnson M W and Moore J 1983 *J. of Engineering Power* **105** (1) 24

[13] Krain H 1988 *J. of Turbomachinery* **110** 122

[14] Moore J and Moore J G 1980 *Three-Dimensional, Viscous Flow Calculations for Assessing the Thermodynamic Performance of Centrifugal Compressors – Study of the Eckardt Compressor* AGARD-CP-282

[15] Casey W V, Dalbert P and Roth P 1992 *J. of Turbomachinery* **114** 27

[16] Denton J D 1986 *The Use of a Distributed Body Force to Simulate Viscous Effects in 3D Flow Calculation* ASME Paper 86-GT-144

[17] Dawes W N 1988 *Development of 1 3D Navier-Stokes for Application to all Types of Turbomachinery* ASME Paper 88-GT-70

[18] Dawes W N 1995 *Unsteady Flow and Loss Production in Centrifugal and Axial Compressor Stages* AGARD-PEP Paper (37)

[19] Hah C and Krain H 1990 *J. of Turbomachinery* **112** 7

[20] Johnson M W and Moore J 1983 *J. of Engineering Power* **105** (1) 33

[21] Chriss R M, Hathaway M D and Wood J R 1996 *J. of Turbomachinery* **118** 55

[22] Kang S and Hirsch Ch 1999 *Effects of Flow Rate on the Development of Three-Dimensional Flow in NASA LSCC Impeller, Based Numerical Solutions* ISABE Paper 99-7225

[23] Hirsch Ch, Kang S and Pointet G 1996 *A Numerically Supported Investigation on the 3D Flow in Centrifugal Impellers. Part I: The Validation Base* ASME Paper 96-GT-151

[24] Hirsch Ch, Kang S and Pointet G 1996 *A Numerically Supported Investigation on the 3D Flow in Centrifugal Impellers. Part II: Secondary Flow Structure* ASME Paper 96-GT-152

[25] Kang S and Hirsch Ch 1996 *Influence of Tip Leakage Flow in Centrifugal Compressor* 3^{rd} ISAIF, Beijing, pp. 186–194

[26] Kang S and Hirsch Ch 1999 *Numerical Investigation of the Three-Dimensional Flow in MASA Low-Speed Centrifugal Compressor Impeller* 4^{th} ISAIF, Dresden, Germany, pp. 274–284

[27] Acosta A J and Bowerman R D 1957 *An Experimental Studay of Centrifugal Pump Impellers* Trans. ASME, pp. 1821–1839

[28] Van den Braembussche R 1985 *Description of Secondary Flow in Radial Flow Machines* Published in Thermodynamics and Fluid Mechanics of Turbomachinery Volume II, Edited by Ucer A S, Stow P and Hirsch Ch, NATO ASI Series, pp. 665–684

[29] Johnson M W 1978 *J. of Engineering Power* **100** 553
[30] Hathaway M D, Chriss R M, Strazisar A J and Wood JR 1995 *Laser Anemometer Measurements of the Three-Dimensional Rotor Flow Field in the NASA Low-Speed Centrifugal Compressor* NASA Technical Paper ARL-TR-333
[31] Hirsch Ch, Lacor C, Dener C and Vucinic D 1992 *An Integrated CFD System for 3D Turbomachinery Applications* AGARD-CP-510
[32] Yang Z and Shih T H 1993 *AIAA Journal* **31** (7) 1191
[33] Khodak A and Hirsch Ch 1996 *Second Order Non-Linear k-ε Models with Explicit Effect of Curvature and Rotation* Computational Fluid Dynamics'96, Proceeding of the Third ECCOMAS Computational Fluid Dynamics Conference, pp. 690–696
[34] Hah C, Bryans A C, Moussa Z and Tomsho M E 1988 *J. of Turbomachinery* **110** 303